Received: 19 April 2018 | Revised: 3 June 2018 | Accepted: 11 July 2018

DOI: 10.1002/jbio.201800147

Journal of BIOPHOTONICS

FULL ARTICLE

Miniature probe for all-optical double gradient-index lenses photoacoustic microscopy

Zhendong Guo[1] | Guangyao Li[1] | Sung-Liang Chen[1,2]*

[1]University of Michigan-Shanghai Jiao Tong University Joint Institute, Shanghai Jiao Tong University, Shanghai, China

[2]State Key Laboratory of Advanced Optical Communication Systems and Networks, Shanghai Jiao Tong University, Shanghai, China

***Correspondence**
Sung-Liang Chen, University of Michigan-Shanghai Jiao Tong University Joint Institute, Shanghai Jiao Tong University, Shanghai 200240, China.
Email: sungliang.chen@sjtu.edu.cn

Funding information
National Natural Science Foundation of China (NSFC), Grant/Award Number: 61775134

A novel all-optical double gradient-index (GRIN) lens optical-resolution photoacoustic microscopy (OR-PAM), termed as DGL-PAM, is demonstrated. The miniature probe consists of a single-mode fiber and double GRIN lenses for optical focusing and a miniature fiber Fabry-Perot sensor for ultrasound detection. The new design is simple and realizes high resolution with long working distance (WD) by virtue of the double GRIN lenses. The overall size of the probe is 2.7 mm in diameter. High lateral resolution of 3.7 μm (at 532 nm laser wavelength) and long WD of 5.5 mm are achieved. *In vivo* OR-PAM of mouse ear demonstrates the imaging ability of DGL-PAM. Since precise alignment of optical and acoustic foci is not needed, the proposed DGL-PAM is relatively easy to implement. It has potential to be developed as a low-cost, disposable OR-PAM probe and for endoscopic applications. The proposed double GRIN lenses for making miniature endoscopic probes can also be applied to other modalities, such as optical coherence tomography and confocal fluorescence microscopy, to enable high resolution and long WD.

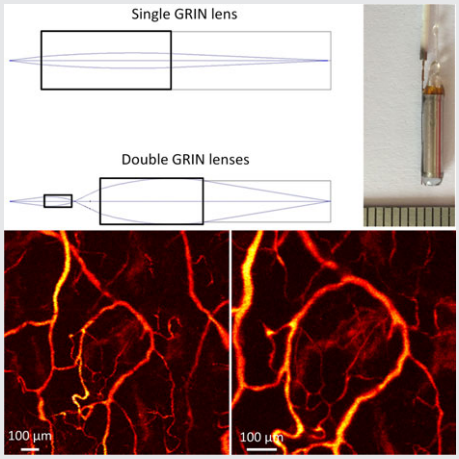

KEYWORDS

all optical, Fabry-Perot, gradient-index lens, photoacoustic imaging, photoacoustic microscopy

1 | INTRODUCTION

Photoacoustic imaging is an attractive imaging technique since it combines the strengths of plentiful optical absorption contrast and low acoustic scattering in biological tissue. Photoacoustic imaging has been explored in a range of applications in biomedicine [1]. In photoacoustic imaging, the biological tissue is irradiated by a pulsed laser beam to engender an acoustic pulse due to thermoelastic expansion. Currently, the major implementations of photoacoustic imaging are photoacoustic computed tomography (PACT) [2], photoacoustic microscopy (PAM) [3–5] and photoacoustic endoscopy (PAE) [6]. PAM aims to provide high-resolution imaging and can be categorized into two types. In optical-resolution PAM (OR-PAM), high lateral resolution (several μm) is enabled by optical focusing, while in acoustic-resolution PAM, acoustic focusing is used to provide lateral resolution (tens to hundreds of μm) at depths to several millimeters. By virtue of its high resolution, OR-PAM is particularly useful in applications such as imaging

microvasculature at capillary level and auscultating biological systems at cellular level [7, 8]. To achieve such high resolution with satisfactory performances such as high sensitivity, long working distance (WD) and reflection-mode operation, sophisticated design and implementation of the imaging head as well as its components are required.

OR-PAM has two schemes: transmission mode and reflection mode. In transmission mode, laser excitation and ultrasound detection are at the opposite sides of objects, and thus, diffraction-limited focusing can be achieved without much difficulty using an objective lens with a high numerical aperture (NA) [9, 10]. However, *in vivo* applications are highly impeded due to usually thick tissue or even a body, which causes much acoustic attenuation for excited photoacoustic waves to propagate to the detection side. By contrast, reflection mode with laser excitation and ultrasound detection at the same sides of objects facilitates *in vivo* studies. However, in reflection mode, the ultrasonic detector is typically not transparent to the excitation wavelength and thus cannot be simply placed above or below the objective lens. Acoustically, placing the ultrasonic detector above the objective lens spoils efficient coupling of ultrasound to the detector since the objective lens generally has acoustic impedance mismatch with tissue. Therefore, efforts have been made in improved combination of laser focusing for high resolution and ultrasound detection for high sensitivity.

There have been four methods explored for the optical-acoustic combination for reflection-mode OR-PAM. (1) An optical-acoustic combiner was used to reflect the optical or acoustic beam so that confocal and coaxial alignment can be effectively realized [4, 11, 12]. However, the combiner is usually big, resulting in longer focal length and thus the smaller NA of the optical focusing. That is, high resolution is sacrificed. Moreover, skillful alignment of optical and acoustic foci is required to optimize the sensitivity. (2) Off-axis method was employed by placing the ultrasound transducer in an oblique direction [13, 14], which degrades the axial resolution and results in a relatively large imaging head if housed. (3) A hollow focused ultrasound transducer was custom made to allow confocal and coaxial optical-acoustic alignment by utilizing the hole of the hollow transducer for laser transmission [15–17], yet the design suffers from the tradeoff between resolution and sensitivity determined by the hole size of the transducer. A small hole hampers high-NA optical focusing for high resolution, while a large hole impairs high sensitivity. (4) A reflective objective lens has a dark zone to allow direct placement of the transducer below the objective without degrading optical focusing [18, 19]. However, the cost is much higher than a refractive-based objective.

As an alternative to piezoelectric transducers, optical detection of ultrasound is a promising method in OR-PAM [20–25]. Optical resonance is utilized to realize sensitive ultrasound detection. For instance, noise-equivalent pressure (NEP) of 8 Pa over bandwidth of 20 MHz was demonstrated by a fiber Fabry-Perot (FP) ultrasound sensor [26]. Bandwidth up to 80 MHz has also been achieved [27]. Photoacoustic imaging based on the fiber FP sensor has been extensively investigated [23, 28, 29]. For another example, a microring resonator with NEP of 105 Pa over ultrabroad bandwidth of 350 MHz has been reported [30], and promising applications of microrings including PACT [31], OR-PAM [20, 21], PAE [22], ultrasound imaging [32] and even the detection of THz pulse radiation have been demonstrated [33]. Particularly, several unique features of the fiber FP ultrasound sensor render it an excellent detector for OR-PAM, including high sensitivity for high-quality imaging, broad bandwidth for high axial resolution, wide-angle detection for circumventing precise alignment, and miniature size for easy integration.

Gradient-index (GRIN) lenses have been used to build miniature OR-PAM probes [16, 17, 22, 34–36]. A GRIN lens with an imaging fiber bundle was used for focusing and scanning the laser beam [34]. Although high resolution of 6 μm is achieved, a relatively short WD of 2 mm may restrict some specific *in vivo* applications such as brain imaging, where long WD with high resolution is desired [18]. Furthermore, the demonstrated probe using a piezoelectric transducer can only operate in transmission mode. The others employed a GRIN lens with a single-mode fiber (SMF) [16, 17, 22, 35]. The best achieved resolution is 9.2 μm with WD of 4.4 mm (from the imaging head to the optical focus) [17]. However, compared with the method of the optical-acoustic combiner [4, 11, 12], there still exists more than 3-fold degradation in resolution (9.2 vs <3 μm [11]). We recently demonstrated a miniature probe using twin GRIN lenses and a hollow transducer to achieve high resolution of 3.1 μm, yet suffered from short WD of 1.4 mm [36]. This is mainly limited by the small size of the GRIN lenses constrained by the small hole of the hollow transducer.

In this work, we demonstrate a miniature OR-PAM probe using double GRIN lenses, which is termed DGL-PAM. Compared with a single GRIN lens or twin GRIN lenses [36], the double GRIN lenses with optimized design provide both high resolution of 3.7 μm and long WD of 5.5 mm. Because the miniature fiber FP ultrasound sensor is employed in this probe, optimization of double GRIN lenses becomes possible. Moreover, the fiber FP sensor has wide-angle ultrasound detection, which facilitates easy integration. The proposed DGL-PAM is a new approach to implement the reflection-mode OR-PAM imaging head. Specifically, in contrast to existing methods with reflection-mode operation, DGL-PAM imaging head has advantages: (1) both high resolution and long WD, (2) miniature size (2.7 mm) with potential for endoscopic applications, (3) simple implementation, (4) low cost and (5) light weight. The above advantages are not simultaneously possessed by the existing

methods. The all-optical scheme is advantageous in immunity against electromagnetic interference.

2 | METHODS

2.1 | DGL-PAM design and optimization

Theoretically, the optical diffraction-limited lateral resolution can be expressed as

$$\text{Resolution} = 0.51\frac{\lambda}{\text{ENA}}, \quad (1)$$

where λ denotes the laser wavelength and ENA denotes the effective NA for the optical focusing. The theoretical lateral resolution corresponds to full width at half maximum (FWHM) of the point spread function in imaging. ENA is determined by the expression:

$$\text{ENA} = n\frac{D}{2f}, \quad (2)$$

where n is the refractive index of the medium where the lens is working, D is the optical beam size on the lens and f is the distance from the lens to the optical focus (ie, WD). Thus, for a fixed λ, n and D, there is a trade-off relation between resolution and WD.

In conventional OR-PAM, high resolution with long WD can be achieved with a large D by using a common focusing lens with a large aperture. By contrast, in miniaturized OR-PAM, a single GRIN lens is typically used, and high resolution and/or long WD are sacrificed. As mentioned above, the best achieved resolution is 9.2 μm with WD of 4.4 mm [17]. There are mainly two reasons: (1) the NA of commercially available SMFs at visible wavelengths is low (0.10-0.14); (2) the D is limited to <1 mm due to the small hole of the hollow transducer. Hence, to optimize the resolution and WD, we equivalently employ a high-NA SMF by using a common low-NA SMF and a 0.5 mm GRIN lens (GL1) and adopt a 2 mm GRIN lens (GL2) for light focusing. The latter is allowed because a miniature fiber FP sensor is used for ultrasound detection.

It is clear that the 2 mm GL2 is helpful to improve resolution and WD by Eqs. (1) and (2). On the other hand, to illustrate the advantages of adding the intermediate GL1, we perform Zemax simulation to compare the cases of using the GL2 alone (a single GRIN lens) and using GL1 and GL2 (double GRIN lenses). A schematic of the two cases is shown in Figure 1A, where d_1 is the distance between the SMF and the input of GL2 in the case of a single GRIN lens. Besides, d_2, d_3 and d_4 are the distance between the SMF and the input of GL1, that between the output of GL1 and the focus after GL1, and that between the focus after GL1 and the input of GL2, respectively, in the case of double GRIN lenses. θ_1 is the divergence angle related to the focus after GL1. The following parameters are used: the common SMF (NA = 0.12), the 0.5 mm GL1 (pitch = 0.25; NA = 0.54), the 2 mm GL2 (pitch = 0.23; NA = 0.51), and design wavelength of 532 nm. Besides, the surrounding before the input of GL2 is the air, while that after GL2 is water (ie, n = 1.33

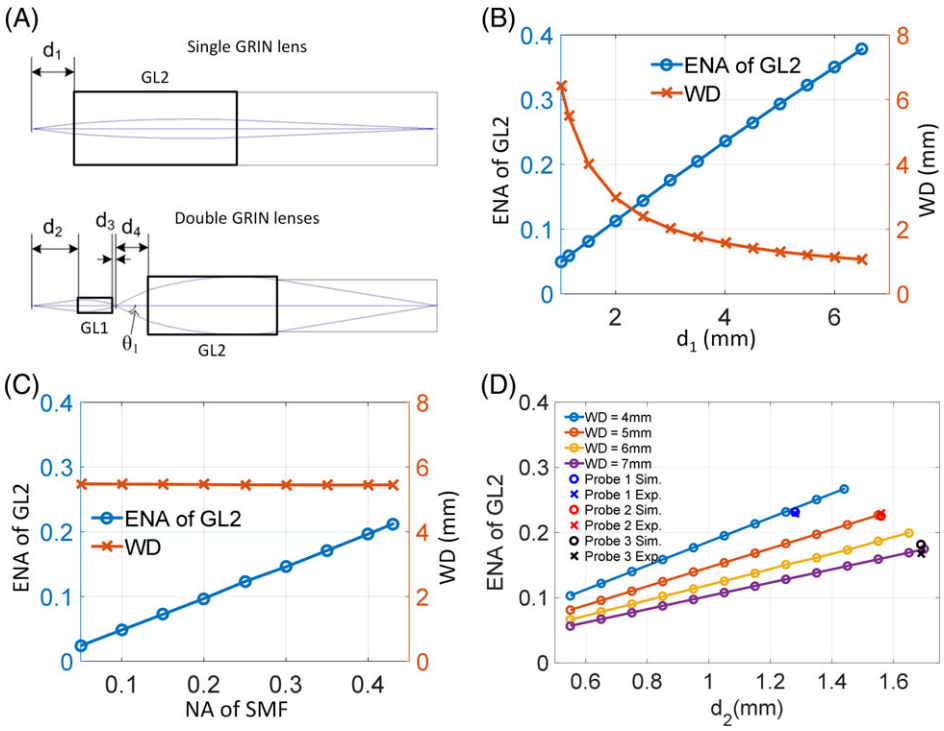

FIGURE 1 DGL-PAM design and optimization. (A) Schematic of the two cases of a single gradient-index (GRIN) lens and double GRIN lenses. (B) Effective numerical aperture (ENA) of GL2 and working distance (WD) as a function of d_1 (the case of a single GRIN lens). (C) ENA of GL2 and WD as a function of the NA of single-mode fiber (SMF). (D) ENA of GL2 as a function of d_2 (the case of double GRIN lenses)

in Eq. (2)). These parameters and surroundings are also used in experiments.

Figure 1B shows the result of the case of a single GRIN lens. As can be seen, by increasing the distance d_1 from 1 to 6.5 mm, ENA (and thus resolution) is enhanced linearly at the cost of WD. For example, at d_1 of 3.6 mm, ENA can be 0.21 with very short WD of 1.7 mm. On the other hand, to enable long WD, ENA is sacrificed. One representative result is that when d_1 is 1.14 mm, the ENA reduces to only 0.058 (corresponding to theoretical resolution of 4.7 μm [= $0.51 \times 0.532/0.058$]) at WD of ~5.5 mm. As a matter of fact, a high-NA SMF can enhance ENA (and thus resolution) while keeping almost the same WD. To illustrate this, we further perform simulation by increasing the NA of SMF from 0.05 to 0.43 at a fixed d_1 of 1.14 mm. The result is shown in Figure 1C. As can be seen, ENA can be enhanced from 0.024 to 0.21, corresponding to theoretical resolutions from 11.3 to 1.3 μm. Note that the long WD of ~5.5 mm is kept, as shown in Figure 1C. As a comparison, at WD of ~5.5 mm, ENA and theoretical resolution are improved by ~3.6 times (ENA: from 0.058 to 0.21; theoretical resolution: from 4.7 to 1.3 μm) when changing the NA of SMF from 0.12 to 0.43.

To our knowledge, high-NA SMFs at visible wavelengths are not commercially available. Fortunately, high-NA (or wide-angle) emitted light can be equivalently realized by using the common low-NA SMF and GL1, which is illustrated in the following. As shown in the case of double GRIN lenses in Figure 1A, the laser emitted from the SMF is focused by GL1 and is then diverged after passing the focus. By increasing d_2, the divergence angle (θ_1) can be enlarged compared with that right after the SMF. That is, the NA of the SMF is equivalently enlarged by the introduction of GL1. Then, the laser after GL1 is further focused by GL2. Thus, as simulated in Figure 1C, high resolution with long WD can be enjoyed compared with the case of a single GRIN lens.

To find out the optimized design of DGL-PAM, we perform the simulation of ENA of GL2, which is directly related to resolution, as a function of d_2 at different desired WD, as shown in Figure 1D. In this simulation, for a certain WD, d_4 is almost fixed, and d_3 is determined according to d_2. That is, d_3 and d_4 are determined according to d_2 and desired WD and thus are not variables. Note that the maximum value of d_2 for each desired WD is determined due to light leakage at GL2. Specifically, as mentioned, d_4 is almost fixed for a desired WD. As d_2 increases, θ_1 will increase and start to cause partial light leakage from the edge of GL2. Thus, the maximum value of d_2 is determined by the maximum θ_1 without light leakage at GL2. The results show that ENA of GL2 (and resolution) will be enhanced as increasing d_2 at a certain WD. That is, the optimal ENA of GL2 (and resolution) can be achieved by using the maximum d_2, corresponding to the rightest points for each WD in Figure 1D. As can be seen in Figure 1D, although the trade-off between optimal resolution and WD still exists in the case of double GRIN lenses, one can have higher resolution while keeping the same longer WD. For example, considering WD of ~5.5 mm, the optimal ENA of GL2 by using double GRIN lenses is 0.21 from this simulation (not shown in Figure 1D), and thus, theoretical resolution can be improved by ~3.6 times (ENA of GL2: from 0.058 to 0.21 by using a single GRIN lens and double GRIN lenses, respectively).

TABLE 1 Comparison of simulation and experimental results of DGL-PAM probe

Probes		d_2 (mm)	$d_3 + d_4$ (mm)	ENA	WD (mm)
1	Simulation	1.28	1.63	0.23	4.08
	Experiment			0.23	3.96
2	Simulation	1.56	1.34	0.23	5.05
	Experiment			0.23	5.15
3	Simulation	1.69	1.05	0.18	6.7
	Experiment			0.17	6.65

Abbreviations: ENA, effective numerical aperture; WD, working distance.

We made three different DGL-PAM probes (details described later), measured the ENA and WD, and compared the experimental results with the simulation, which is shown in Table 1 and Figure 1D. Here, we chose different d_2 and $d_3 + d_4$ in order to obtain the probes with WD ranging from ~4 to 7 mm. Note that d_2 and $d_3 + d_4$ in the simulation are chosen the same as those measured in experiments. As shown in Table 1 and Figure 1D, both the ENA and WD show excellent consistency between the simulation and experimental results.

3 | PROBE FABRICATION

3.1 | DGL-PAM probe

A schematic of the DGL-PAM probe is shown in Figure 2A. In this probe, an SMF (S405-XP, Nufern, East Granby, Connecticut), denoted as SMF1, for wavelengths of 400 to 680 nm with an NA of 0.12 was used to deliver 532-nm laser pulses. Then, GL1 (GT-LFRL-050-025-50-CC (532), GRINTECH) with a diameter of 0.5 mm was placed after the SMF1. The SMF1 and GL1 were fixed by a glass tube. The distance between SMF1 and GL1 (d_2) was ~1.6 mm. The divergence angle (θ_1) up to ~26° (NA: ~0.44) was measured. GL2 (GT-LFRL-200-023-50-CC (532), GRINTECH) with a diameter of 2 mm as an objective lens was further utilized to focus the laser beam for photoacoustic excitation. GL2 and the glass tube consisting of SMF1 and GL1 were fixed by a metal ferrule with an outer diameter (OD) of 2.5 mm. Aided by GL1, ENA of GL2 was measured to be ~0.21 and a long WD (f) of 5.5 mm was obtained. For photoacoustic detection, a home-made fiber FP ultrasound sensor was used and attached adjacent to the

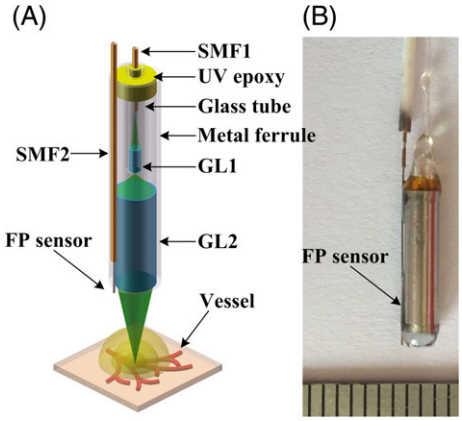

FIGURE 2 (A) Schematic of DGL-PAM probe. (B) Photograph of DGL-PAM probe

metal ferrule. The fiber FP sensor is an optical resonant cavity, consisting of a polymer film in thickness sandwiched between a pair of gold mirrors, on the tip of a standard SMF (SMF-28e+), denoted as SMF2. Figure 2B shows the picture of the fabricated DGL-PAM probe with size of 2.7 mm.

3.2 | FP ultrasound sensor

As mentioned above, to detect the excited photoacoustic waves, the fiber FP ultrasound sensor was used. The fabrication, working system, and ultrasound detection characteristics of the home-made FP sensor have been introduced and detailed in our previous work [29]. Briefly, the FP cavity was made of a polymer film sandwiched between a pair of gold mirrors. First, the gold mirror was deposited on the tip of a standard SMF (SMF-28e+) by sputter coating. Then, the polymer of ~38 μm was dip coated to form a plano-convex spacer. Finally, the second gold mirror was deposited using the same process as the first mirror. A parylene-C film with a thickness of ~5 μm was coated for protection of the fiber-tip FP structure. The diameter of the FP sensor was ~130 μm.

3.3 | Assembly of DGL-PAM probe

The procedure of assembling the DGL-PAM probe is shown in Figure 3. We performed the assembly under a modified microscope system, as shown in Figure 3. We used 3D stages and kinematic mounts (GCM100302M, Daheng Optics, China) for precise adjustment of the components.

First, an SMF1 was mounted on Part 2 in Figure 3A. The center of the output beam from the SMF1 was aligned to the center of a target, as shown in Step 1 in Figure 3B.

Second, optical adhesive (NOA61, Thorlabs, Newton, New Jersey) was used to fix a glass tube (inner diameter [ID]: 0.55 mm, OD: 0.85 mm) and GL1. Then, the part consisting the glass tube and GL1 was mounted on Part 3 in Figure 3A. Next, d_2 was adjusted to the designed value. The center of the output beam after GL1 was aligned to the

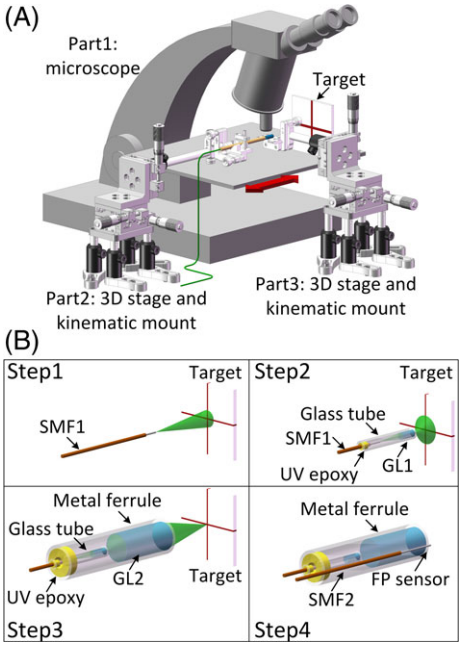

FIGURE 3 Assembly of the DGL-PAM probe. (A) Modified microscope system. (B) Illustration of the four steps for assembling DGL-PAM probe

center of the target, as shown in Step 2 in Figure 3B. After that, the optical adhesive was used to fix the SMF1 and the glass tube.

Third, the optical adhesive was used to fix a steel ferrule (ID: 2.05 mm, OD: 2.5 mm) and GL2. Then, the part consisting the steel ferrule and GL2 was mounted on Part 3 in Figure 3A. Next, ENA of GL2 was adjusted to the designed value, and $d_3 + d_4$ was decided accordingly. The focus after GL2 was aligned to the center of the target, as shown in Step 3 in Figure 3B. After that, the optical adhesive was used to fix the glass tube and the steel ferrule. It is important that the SMF1, GL1, GL2, and the target should be placed coaxially in the above three procedures.

Fourth, the FP sensor (SMF2) was attached adjacent to the steel ferrule, as shown in Step 4 in Figure 3B.

4 | RESULTS

4.1 | Experimental setup

The experimental setup for the DGL-PAM probe is shown in Figure 4. A 532 nm pulsed laser (FDSS532-Q3, CryLas, Berlin, Germany) with a repetition rate of 1 kHz was used for photoacoustic excitation. The laser was attenuated, spatially filtered, and coupled into the SMF1. As for the detection system, the FP sensor was probed using a continuous wave tunable laser (HP 8168F, Agilent, Santa Clara, California) with a wavelength range of 1450 to 1590 nm. A fiber circulator was used to access the input and output ports of the FP sensor via SMF2. The output port collecting the reflected light was further connected to a 1 × 2 fiber coupler with a power ratio of 10:90. The 10% reflected power was

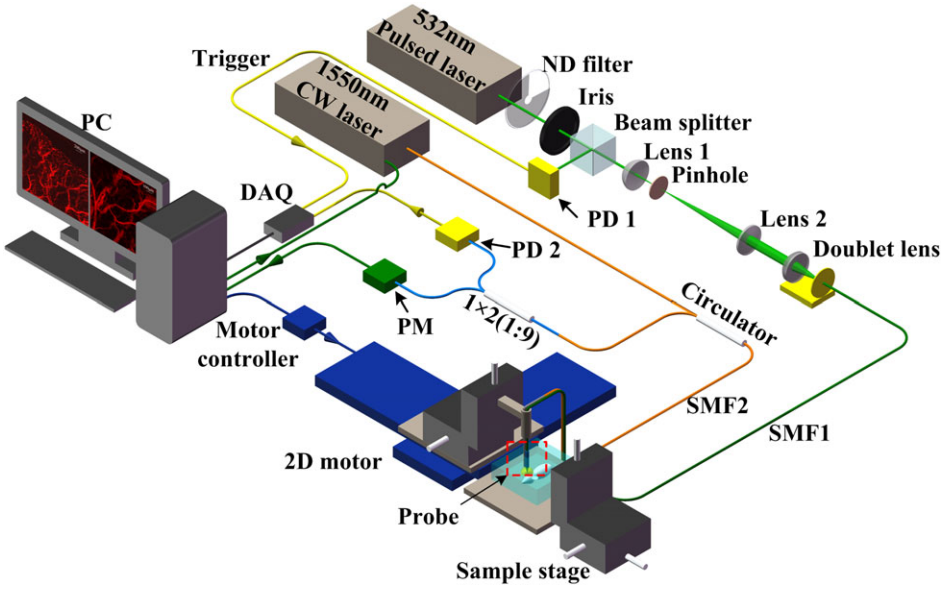

FIGURE 4 Experimental setup for DGL-PAM probe. ND, neutral density; PC, personal computer; PD, photodetector; PM, power meter

measured by a power meter (2832-C, Newport, Irvine, California) to obtain the FP cavity's reflection spectrum, and the 90% reflected power was detected using a photodetector (1811-FC-AC, New Focus) with an output gain of 40 V/mA and electrical bandwidth of 25 kHz to 125 MHz to capture the short modulated optical pulses induced by the incoming photoacoustic pulses. During the FP operation, we first scanned the wavelengths of the tunable laser to get the interferometer transfer function (ITF). A fixed wavelength was then chosen at the highest slope of the ITF, which consequently translated into high intensities of the ultrasound-modulated optical pulses. Therefore, a sharp slope provided by high-quality FP sensor enables high-sensitivity ultrasound detection. The device has an NEP of ~0.33 kPa over bandwidth of 15 MHz at −10 dB. Note that a very low NEP of 8 Pa over a bandwidth of 20 MHz has been reported [26], which means that the sensitivity of our DGL-PAM probe can be further improved by more than 40 times in the future. The photoacoustic signals were sampled by a high-speed digitizer (CSE1422, Gage, Lockport, Illinois) with a sampling rate of 200 MS/s and 14-bit resolution. The DGL-PAM probe was mounted on a two-dimensional (2D) motorized stage (M-404, Physik Instrumente [PI]) for scanning during image acquisition.

4.2 | Resolution and imaging depth

Lateral resolution of the DGL-PAM probe is determined by the focal spot size after GL2. A sharp edge of a razor blade in water was imaged to calibrate the lateral resolution. A step size of 0.5 μm was used in scanning across the sharp edge. A one-dimensional (1D) photoacoustic amplitude profile was obtained and fitted by a sigmoidal-shaped curve as the fitted edge spread function (ESF) [37]. The line spread function (LSF) can be calculated by taking the spatial derivative of the ESF. The 1D photoacoustic profile, the fitted ESF and the calculated LSF are shown in Figure 5A. The FWHM of the LSF was used to determine the lateral resolution, which was estimated as 3.7 μm. Meanwhile, the WD was measured as ~5.5 mm. As mentioned above, the ENA was ~0.21, which results in theoretical diffraction-limited lateral resolution of 1.3 μm [= 0.51 × (0.532 μm)/0.21]. As a comparison, the measured value is much worse than the theoretical one, which is probably due to optical aberration of the GRIN lenses. The exact reason is under investigation. We also made a probe consisting of SMF1 and a single GRIN lens GL2, and lateral resolution of 9.5 μm at WD of ~5.5 mm was measured (results not shown), which experimentally confirms the advantage of using double GRIN lenses over a single GRIN lens. The axial resolution of the DGL-PAM probe was determined by imaging a 6-μm carbon fiber. A photoacoustic temporal signal and its Hilbert transform (envelope detection) are shown in Figure 5B. The axial resolution was measured as 68 μm by taking the FWHM of the envelope. To measure the imaging depth of our DGL-PAM probe, a needle with a diameter of 250 μm obliquely inserted into chicken breast was imaged. Another same needle placed on the surface of the chicken breast was used as a reference. A photograph of the sample is shown in Figure 5C. The pulse energy used in this calibration was measured as ~510 nJ. As shown in Figure 5D, the DGL-PAM probe can clearly visualize the needle down to 0.38 mm (determined by signal-to-noise ratios (SNRs) >10 dB) beneath the reference surface. Therefore, the imaging depth is determined to be better than 0.38 mm in biological tissue. Penetration depth can be further enhanced by using the FP sensor with higher sensitivity.

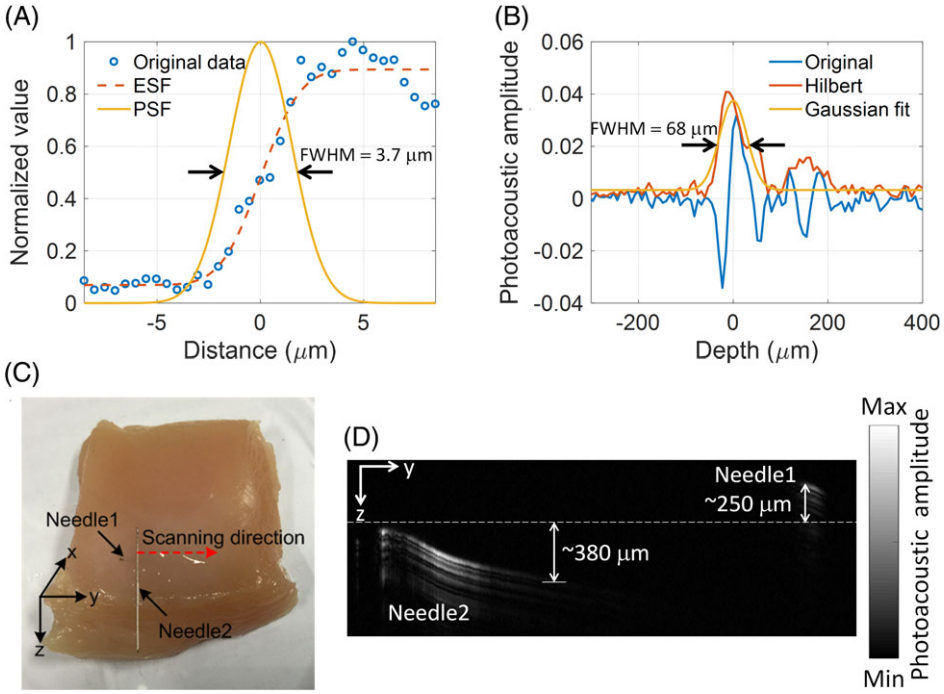

FIGURE 5 (A) Calibration of lateral resolution. (B) Calibration of axial resolution. (C) Photograph of the sample of the black needle obliquely inserted into chicken breast (Needle1) and the needle on the surface of the chicken breast as a reference (Needle2). (D) Optical-resolution photoacoustic microscopy (OR-PAM) of (C) for calibration of imaging depth

4.3 | Imaging of a leaf

To assess the imaging performance of the system, a phantom of a leaf skeleton dyed with black ink was imaged. The phantom was covered by a layer of epoxy to protect the ink from leaking out of the leaf skeleton. Figure 6A is a photograph of the leaf phantom. A region of 3.8 mm × 4 mm (red dashed box in Figure 6A) was imaged, and the 2D maximum amplitude projection (MAP) image is shown in Figure 6B. As can be seen, veins with different diameters (~30−250 μm) were clearly imaged. Besides, the PAM image and the photograph have high resemblance.

4.4 | *In vivo* imaging of a mouse ear

The 6~8 weeks old mouse (BALB/c, Jiesijie, Shanghai, China) was anesthetized with pentobarbital and placed on a home-made animal platform. Before the experiment, the hair on the ear of the mouse was gently removed using a human-hair removing cream. All experimental animal procedures were carried out in conformity with the laboratory animal protocol approved by Laboratory Animal Care Committee of Shanghai Jiao Tong University.

To demonstrate the *in vivo* imaging capability of the DGL-PAM probe, a mouse ear was imaged. The laser pulse energy at the surface of the sample was ~510 nJ. By adjusting the optical focus at ~0.1 mm below the skin surface, the surface laser fluence can be estimated as 63 mJ/cm^2 [= (510 nJ)/(π × ((0.1 mm)×0.16)^2)], which is higher than the American National Standards Institute safety limit (20 mJ/cm^2 for the visible wavelengths), but still below the damage threshold (200 mJ/cm^2) [17]. An area of 1.25 mm × 1.25 mm of the mouse ear was imaged with scanning step size of 5 μm (i.e., 250 × 250 scanning points). Signal averaging of 16 times was used to enhance the SNR of images. The 2D MAP image of the microvasculature is shown in Figure 7A, where the morphology of the microvasculature can be clearly observed. Using smaller step size of 3 μm, Figure 7B shows a zoom MAP image in the area indicated by the white dashed box in Figure 7A, and more details of the microvasculature are visualized. After image acquisition, no obvious damage of the mouse ear was found by naked-eye inspection. Figure 7C shows the depth-encoded MAP image on the scanning plane of Figure 7B, demonstrating the three-dimensional (3D) imaging ability of the DGL-PAM probe. Further, single capillaries (eg, indicated by the two white arrows) at superficial layers (colored in blue)

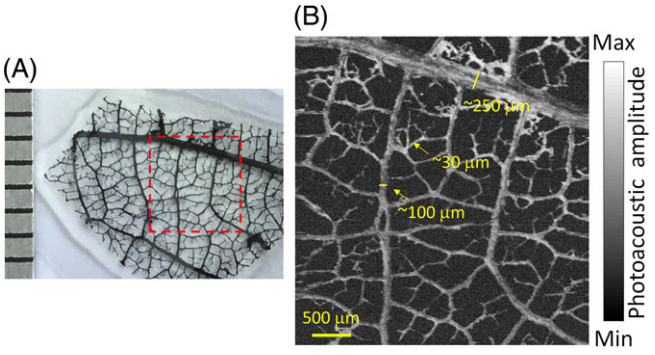

FIGURE 6 Photograph (A) and optical-resolution photoacoustic microscopy (OR-PAM) (B) of leaf phantom

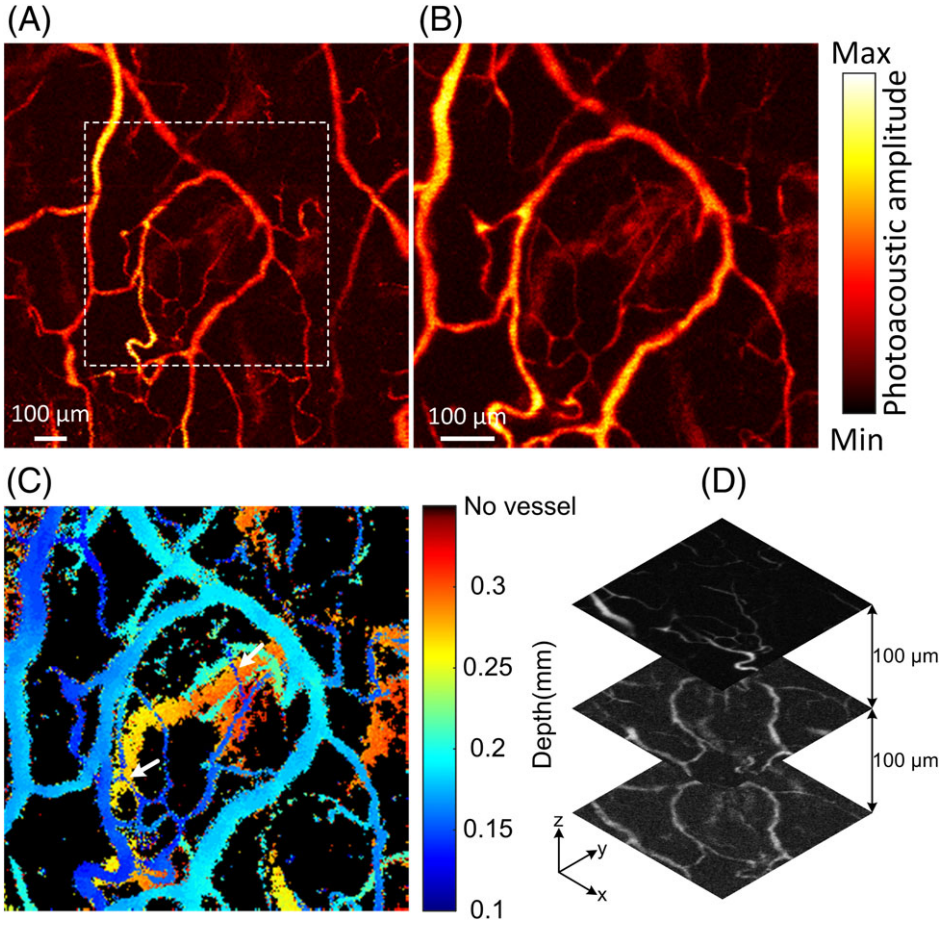

FIGURE 7 (A) *In vivo* optical-resolution photoacoustic microscopy (OR-PAM) (MAP) of mouse ear. (B) OR-PAM (MAP) of the zoom region in the white dashed box in (A). (C) Depth-encoded OR-PAM (MAP) image of (B). (D) Three representative layers at different depths of (B)

overlaying deeper lying vessels (colored in yellow or orange) can be clearly identified. Three representative layers at different depths with separation of 100 μm are shown in Figure 7D.

5 | DISCUSSION AND CONCLUSION

In our design of the DGL-PAM probe, we used two GRIN lenses, GL1 and GL2. GL1 was used to increase the divergence angle (θ_1) before entering GL2 (serving as the objective lens), which enables high resolution with long WD compared with using single GL2 alone. As mentioned above, this is earned by equivalently having a high-NA SMF for the wavelength of 532 nm. To our knowledge, currently the NA of commercially available SMFs for visible wavelengths is low (0.10-0.14), which manifests the value of our design using double GRIN lenses.

Although the FP sensor for photoacoustic imaging has been reported in our previous work [29], simple light illumination (without light focusing) was employed. Thus, resolution of ~100 μm over a large depth range of >4 mm was obtained, which is not suitable for high-resolution imaging applications. By contrast, in this work, major efforts were made on the design and optimization of the double GRIN lenses (as detailed in Section 2.1), which is critical to achieving high-resolution and long-WD light focusing via a miniature part.

Although the resolution and WD are upgraded by the design of double GRIN lenses, the DGL-PAM probe and system should be further improved to facilitate *in vivo* and clinical applications. First, the sensitivity and bandwidth of the fiber FP ultrasound sensor should be improved for better imaging depth, imaging speed and axial resolution. The NEP of 2.1 mPa per $\sqrt{\text{Hz}}$ of the fiber FP ultrasound sensor has been demonstrated [25]. That is, highly sensitive FP sensors with broad bandwidth are technically feasible. In addition, for longer WD, the photoacoustic signal amplitude detected by the FP sensor is reduced due to longer acoustic propagation distance, which causes more attenuation of ultrasound waves. That is, imaging sensitivity will be degraded. The highly sensitive FP sensor also facilitates longer WD with satisfactory imaging sensitivity. Second, imaging speed can also be improved by using a pulsed laser with high repetition rate [11]. Third, the potential design of a side-viewing probe is discussed. As shown in Figure S1, Supporting Information, a rod mirror and a micromotor for rotary scan can be employed to steer both the light beam from the exit of GL2 to the tissue and the photoacoustic wave from the tissue to the FP sensor.

TABLE 2 Comparison of reflection-mode OR-PAM imaging heads

Methods	Resolution (μm)[a]	WD (mm)	Size (mm)[b]	Alignment of optical-acoustic beams	Refs.
Optical-acoustic combiner	2.56	~6	Large	Demanding	[4, 11, 12]
Off-axis	7.8	N/A[c]	Large	Simple	[13, 14]
Hollow focused transducer	0.7 [15]	<7 [15]	N/A[c] [15]	Demanding	[15–17]
	9.2 [17]	4.4 [17]	3.8 [17]		
Reflective objective	1.2	6	Large	Demanding	[18, 19]
Double GRIN lenses and FP sensor	3.7	5.5	2.7	Simple	This work

Abbreviations: FP, Fabry-Perot; GRIN, gradient-index; OR-PAM, optical-resolution photoacoustic microscopy; WD, working distance.
[a] The best resolution is quoted. For the others (columns 3-5), the Ref. cited in Resolution (column 2) is referred to.
[b] Large for those >10 mm.
[c] Not available.

We developed a novel DGL-PAM probe with a compact size of 2.7 mm in diameter by employing double GRIN lenses and the fiber FP ultrasound sensor. By the proposed design and optimization of the double GRIN lenses for laser focusing, lateral resolution of 3.7 μm with long WD of 5.5 mm was experimentally demonstrated. The imaging ability of the DGL-PAM was showcased by imaging of the leaf and mouse ear *in vivo*. To elaborate the advantages of the DGL-PAM probe, Table 2 shows the comparison of reflection-mode OR-PAM imaging heads. As can be seen, both high resolution and long WD were achieved in a miniature imaging probe. As shown in Table 2, the WD in several OR-PAM imaging heads is designed to be from 4.4 to <7 mm. For a fair comparison, WD of 5.5 mm was chosen for the DGL-PAM probe and its imaging demonstrations. Furthermore, the implementation of the DGL-PAM probe is relatively simple. Functional imaging by the DGL-PAM probe will be of great interest for future work. It is worth mentioning that the proposed double GRIN lenses for high resolution and long WD can also be used in other endoscopic modalities, such as optical coherence tomography and confocal fluorescence microscopy.

ACKNOWLEDGMENTS

This work was supported by National Natural Science Foundation of China (NSFC) (61775134).

AUTHOR BIOGRAPHIES

Please see Supporting Information online.

ORCID

Sung-Liang Chen https://orcid.org/0000-0002-0572-5110

REFERENCES

[1] L. V. Wang, *Science* **2012**, *335*, 1458.
[2] X. Wang, Y. Pang, G. Ku, X. Xie, G. Stoica, L. V. Wang, *Nat. Biotechnol.* **2003**, *21*, 803.
[3] H. F. Zhang, K. Maslov, G. Stoica, L. V. Wang, *Nat. Biotechnol.* **2006**, *24*, 848.
[4] K. Maslov, H. F. Zhang, S. Hu, L. V. Wang, *Opt. Lett.* **2008**, *33*, 929.
[5] D. Cai, Z. Li, Y. Li, Z. Guo, S.-L. Chen, *Opt. Express* **2017**, *25*, 1421.
[6] J.-M. Yang, K. Maslov, H.-C. Yang, Q. Zhou, K. K. Shung, L. V. Wang, *Opt. Lett.* **2009**, *34*, 1591.
[7] S.-L. Chen, Z. Xie, P. L. Carson, X. Wang, L. J. Guo, *Opt. Lett.* **2011**, *36*, 4017.
[8] S. Hu, L. V. Wang, *Biophys. J.* **2013**, *105*, 841.
[9] Y. Yuan, S. Yang, D. Xing, *Appl. Phys. Lett.* **2012**, *100*, 023702.
[10] J. Yao, L. Wang, C. Li, C. Zhang, L. V. Wang, *Phys. Rev. Lett.* **2014**, *112*, 014302.
[11] S. Hu, K. Maslov, L. V. Wang, *Opt. Lett.* **2011**, *36*, 1134.
[12] L. Wang, K. Maslov, J. Yao, B. Rao, L. V. Wang, *Opt. Lett.* **2011**, *36*, 139.
[13] Z. Xie, S. Jiao, H. F. Zhang, C. A. Puliafito, *Opt. Lett.* **2009**, *34*, 1771.
[14] R. L. Shelton, B. E. Applegate, *IEEE Trans. Biomed. Eng.* **2010**, *57*, 1835.
[15] D.-K. Yao, K. Maslov, K. K. Shung, Q. Zhou, L. V. Wang, *Opt. Lett.* **2010**, *35*, 4139.
[16] H. Estrada, J. Turner, M. Kneipp, D. Razansky, *Laser Phys. Lett.* **2014**, *11*, 045601.
[17] J.-M. Yang, C. Li, R. Chen, B. Rao, J. Yao, C.-H. Yeh, A. Danielli, K. Maslov, Q. Zhou, K. K. Shung, L. V. Wang, *Biomed. Opt. Express* **2015**, *6*, 918.
[18] H. Wang, X. Yang, Y. Liu, B. Jiang, Q. Luo, *Opt. Express* **2013**, *21*, 24210.
[19] R. Cao, J. P. Kilroy, B. Ning, T. Wang, J. A. Hossack, S. Hu, *Photoacoustics* **2015**, *3*, 55.
[20] Z. Xie, S.-L. Chen, T. Ling, L. J. Guo, P. L. Carson, X. Wang, *Opt. Express* **2011**, *19*, 9027.
[21] H. Li, B. Dong, Z. Zhang, H. F. Zhang, C. Sun, *Sci. Rep.* **2014**, *4*, 4496.
[22] B. Dong, S. Chen, Z. Zhang, C. Sun, H. F. Zhang, *Opt. Lett.* **2014**, *39*, 4372.
[23] T. J. Allen, E. Zhang, P. C. Beard, *Proc. SPIE* **2015**, *9323*, 93230Z.
[24] S.-L. Chen, L. J. Guo, X. Wang, *Photoacoustics* **2015**, *3*, 143.
[25] J. A. Guggenheim, J. Li, T. J. Allen, R. J. Colchester, S. Noimark, O. Ogunlade, I. P. Parkin, I. Papakonstantinou, A. E. Desjardins, E. Z. Zhang, P. C. Beard, *Nat Photonics* **2017**, *11*, 714.
[26] E. Z. Zhang, P. C. Beard, *Proc. SPIE* **2011**, *7899*, 78991F.
[27] E. Z. Zhang, P. C. Beard, *Proc. SPIE* **2015**, *9323*, 932311.
[28] D. Cai, G. Li, D. Xia, Z. Li, Z. Guo, S.-L. Chen, *Opt. Express* **2017**, *25*, 20162.
[29] G. Li, Z. Guo, S.-L. Chen, *Opt. Express* **2017**, *25*, 25023.
[30] C. Zhang, T. Ling, S.-L. Chen, L. J. Guo, *ACS Photonics* **2014**, *1*, 1093.
[31] S.-L. Chen, T. Ling, L. J. Guo, *J. Biomed. Opt.* **2011**, *16*, 056001.
[32] B.-Y. Hsieh, S.-L. Chen, T. Ling, L. J. Guo, P.-C. Li, *Photoacoustics* **2014**, *2*, 39.
[33] S.-L. Chen, Y.-C. Chang, C. Zhang, J. G. Ok, T. Ling, M. T. Mihnev, T. B. Norris, L. J. Guo, *Nat. Photonics* **2014**, *8*, 537.
[34] P. Hajireza, W. Shi, R. Zemp, *Laser Phys. Lett.* **2013**, *10*, 055603.
[35] X. Bai, X. Gong, W. Hau, R. Lin, J. Zheng, C. Liu, C. Zeng, X. Zou, H. Zheng, L. Song, *PLoS One* **2014**, *9*, e92463.
[36] Z. Guo, Y. Li, S.-L. Chen, *Opt. Lett.* **2018**, *43*, 1119.
[37] J. M. Boone, J. A. Seibert, *Med. Phys.* **1994**, *21*, 1541.

SUPPORTING INFORMATION

Additional supporting information may be found online in the Supporting Information section at the end of the article.

Figure S1 Potential design of a side-viewing DGL-PAM probe.

How to cite this article: Guo Z, Li G, Chen S-L. Miniature probe for all-optical double gradient-index lenses photoacoustic microscopy. *J. Biophotonics*. 2018; 11:e201800147. https://doi.org/10.1002/jbio.201800147